MAVEN Observations of H– Ions in the Martian Atmosphere

N. Jones, J. Halekas, Z. Girazian, D. Mitchell, C. Mazelle

JGR Planets

RESEARCH ARTICLE
10.1029/2021JE006999

MAVEN Observations of H^- Ions in the Martian Atmosphere

N. Jones[1], J. Halekas[1], Z. Girazian[1], D. Mitchell[2], and C. Mazelle[3]

[1]Department of Physics and Astronomy, University of Iowa, Iowa City, IA, USA, [2]Space Sciences Laboratory, University of California, Berkeley, CA, USA, [3]L'Institut de Recherche en Astrophysique et Planétologie, Toulouse, France

Key Points:

- We observed H^- ions at low altitudes in the Martian atmosphere whose energies and angular distribution matched those of the upstream solar wind
- Fluxes of H^- varied seasonally, with a maximum near perihelion and the southern summer solstice
- We found a ratio of about four percent between H^- density and H^+ density, lower than previously reported ratios

Correspondence to:

N. Jones,
nafj1038@gmail.com

Citation:

Jones, N., Halekas, J., Girazian, Z., Mitchell, D., & Mazelle, C. (2022). MAVEN observations of H^- ions in the Martian atmosphere. *Journal of Geophysical Research: Planets*, *127*, e2021JE006999. https://doi.org/10.1029/2021JE006999

Received 11 JUL 2021
Accepted 6 JUN 2022

Abstract At Mars, charge exchange between solar wind protons and neutral exospheric hydrogen produces energetic neutral atoms (ENAs) that can penetrate into the collisional atmosphere, where they can be converted through collisions into H^+ and H^-. The Mars Atmosphere and Volatile EvolutioN mission observed a population of negatively charged particles at low altitudes, whose energies, angular distribution, and dependence on the upstream solar wind were consistent with H^- produced by solar wind hydrogen ENAs. The highest fluxes of H^- were observed near perihelion and the southern summer solstice. We calculated an average ratio of ~4% between H^- density and H^+ density, implying a slightly smaller relative abundance than reported previously (~10%). We found that the fraction of H ENAs converted to H^- increases with the solar wind energy, in agreement with laboratory measurements of the H–CO_2 electron capture cross section.

Plain Language Summary At Mars, interactions between solar wind protons and neutral hydrogen in the outer atmosphere produces energetic neutral atoms that travel into the inner atmosphere, where collisions with atmospheric gas can produce H^+ ions and H^- ions. The Mars Atmosphere and Volatile EvolutioN mission observed H^- ions in the inner atmosphere, with energies and velocities that matched the solar wind. The highest fluxes of H^- ions were seen when Mars was closest to the Sun, during the southern summer. We found that the relative amount of H^- ions to H^+ ions was smaller than previous studies had found. We also found that the amount of H^- ions produced depended on the solar wind energy, a result that agrees with laboratory experiments.

1. Introduction

In addition to a collisional atmosphere, Mars has a neutral hydrogen exosphere that extends to altitudes of several Martian radii (Anderson, 1974; Chaufray et al., 2008). A portion of the exosphere extends to altitudes upstream of the Martian bow shock, where incoming solar wind protons can undergo charge exchange with neutral exospheric hydrogen to produce energetic neutral atoms (ENAs) moving toward Mars with the original solar wind velocity (Gunell et al., 2006; Holmström, 2002; Kallio et al., 1997). Uninhibited by electromagnetic fields, the ENAs can pass through the bow shock and into the collisional atmosphere, where collisions with atmospheric gases can cause energy deposition (Kallio & Barabash, 2001), proton aurora (Deighan et al., 2018; Ritter et al., 2018), and angular spreading and backscatter (Bisikalo et al., 2018; Girazian & Halekas, 2021; Halekas, Lillis, et al., 2015; Kallio & Barabash, 2001; Shematovich et al., 2011). The ENAs can also undergo electron stripping or electron attachment in collisions with atmospheric neutrals, producing both positive (Halekas, Lillis, et al., 2015; Kallio & Barabash, 2001) and negative (Halekas, Lillis, et al., 2015) hydrogen ions.

Hydrogen ENAs have been observed at Mars by Mars Express (MEX) (Brinkfeldt et al., 2006; Futaana et al., 2006; Gunell et al., 2006; Mura et al., 2008; Wang et al., 2013). However, MEX periapsis altitudes of ~270 km lie above altitudes of peak ENA energy deposition. Mars Atmosphere and Volatile EvolutioN (MAVEN)'s lower altitude periapsis of ~150 km provides an opportunity to observe the charged products of ENA collisions at altitudes of peak energy deposition. Indeed, Halekas, Lillis et al. (2015) observed a ubiquitous flux of H^+ ions and an occasional flux of H^- ions at low altitudes, with energies corresponding to the upstream solar wind. In this manuscript, we more closely examine the H^- ions detected by MAVEN at low altitudes.

Similar effects occur at comet 67P/Churyumov–Gerasimenko, where H^- ions have been detected by the Ion and Electron Sensor aboard Rosetta (Burch et al., 2015). Here, H^- ions were observed with fluxes of ~10% of the proton fluxes and energies of ~90% of the proton energies. Burch et al. (2015) concluded that the observed fluxes and energies were consistent with H^- ion production via double charge exchange between solar wind protons and

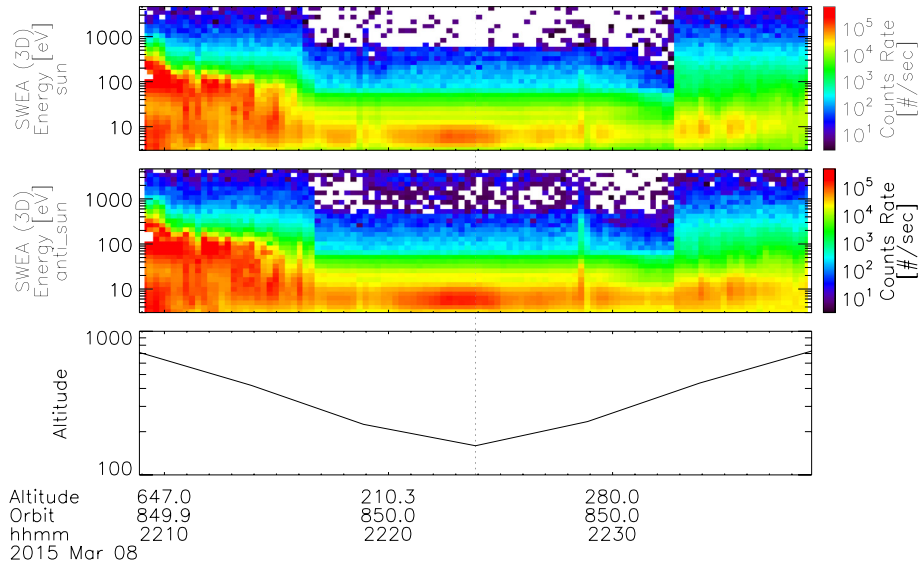

Figure 1. Angle–integrated time–series plots of Solar Wind Electron Analyzer (SWEA) 3D survey data for sunward (top) and anti–sunward (middle) particle velocities, covering 30 min centered on the time of periapsis for a Mars Atmosphere and Volatile EvolutioN orbit on 08 March 2015. The spacecraft altitude (bottom) is also shown. SWEA observed high fluxes of photoelectrons at low energies in both velocity directions. At altitudes below ~200 km, there is low–flux signal at high energies seen exclusively in the anti–sunward velocity direction, which we interpret as H^- ions produced by the solar wind.

molecules in the coma. The study at comet 67P provides a valuable comparison for our own study of H^- ions at Mars.

2. Data

We used data from MAVEN's Solar Wind Electron Analyzer (SWEA) (Mitchell et al., 2016), an electrostatic analyzer that measures negatively charged particles between 3 eV and 4.6 keV. SWEA has an energy resolution of $\Delta E/E = 17\%$, a measurement cadence of 2 s, and a field of view of 360° × 120° (azimuth × elevation) with an angular resolution of 22.5° × 20° (azimuth × elevation). Although designed to measure electrons in the Mars environment, SWEA is capable of detecting any particle with a negative charge and an energy per charge in the detectable range, including the H^- ions of interest in our study.

Our analysis included 3150 MAVEN orbits occurring between 07 October 2014 and 22 February 2020. We required that MAVEN be orbiting on the dayside of Mars during spacecraft periapsis, such that the area of observation was directly downstream of the solar wind. This allowed us to compare SWEA's measurements with the upstream solar wind, which was measured on the same orbits by MAVEN's Solar Wind Ion Analyzer (SWIA) (Halekas, Taylor, et al., 2015). We expect H^- ions produced by solar wind hydrogen ENAs to have energies close to that of the solar wind. Therefore, we filtered out orbits where the upstream solar wind energy was below 600 eV so that H^- ions produced by solar wind hydrogen ENAs would be separated from the significant fluxes of photoelectrons, including Auger electrons at ~500 eV (Mitchell et al., 2000). While Halekas, Lillis et al. (2015), Halekas, Taylor et al. (2015) observed H^+ ions on most orbits, we found that the signal of H^- ions is more rarely seen, and is more tenuous when it is seen. In our analysis, we did not apply any criteria to filter out orbits where H^- ions were not detected. Given the criteria listed above, an H^- signal could have been detected on any of the orbits, and the absence of such a signal is itself a valuable result when considering the general characteristics of these ions.

Figure 1 shows an example of SWEA data from a single periapsis pass on 08 March 2015. The top and middle panels are angle–integrated spectrograms covering 30 min, centered on the time of periapsis, and the bottom panel is a time–series plot of the spacecraft altitude. The top panel is averaged over surface–looking directions and depicts fluxes and energies of particles with sunward velocities, while the middle panel is averaged over space–looking directions and depicts fluxes and energies of particles with anti–sunward velocities. At low

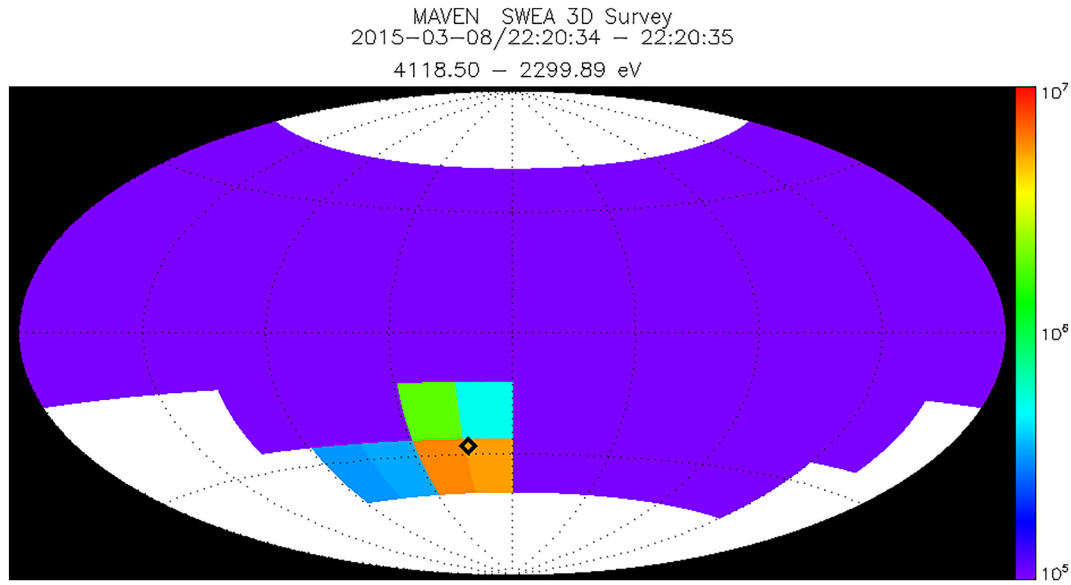

Figure 2. Angular distribution of high-energy (2–4 keV) Solar Wind Electron Analyzer differential energy flux (eV/cm^2 sec sr eV) measured at low altitude. The black diamond indicates the sunward-looking direction (i.e., anti-sunward particle velocities). The space angle is 4π, and counts are collected over the full mass/charge range.

energies, MAVEN observed significant fluxes of electrons in both the sunward and anti–sunward velocity directions. At altitudes below ∼200 km, MAVEN observed a low–flux signal exclusively in the anti–sunward velocity direction, with energies corresponding to the solar wind energy (∼3 keV at this time). Figure 2 shows the corresponding angular distribution of the low-altitude flux measured with energies between ∼2 and ∼4 keV. Nearly all the flux is contained in a narrow angular range, corresponding to the sunward-looking direction (indicated by the black diamond in Figure 2). The low altitude of this signal is indicative of particles produced in the collisional atmosphere, while the high energy and narrow angular range suggests the products of interactions with solar wind particles. Later in this paper we will show that for multiple orbits, the flux of the detected particles is correlated with the upstream solar wind energy.

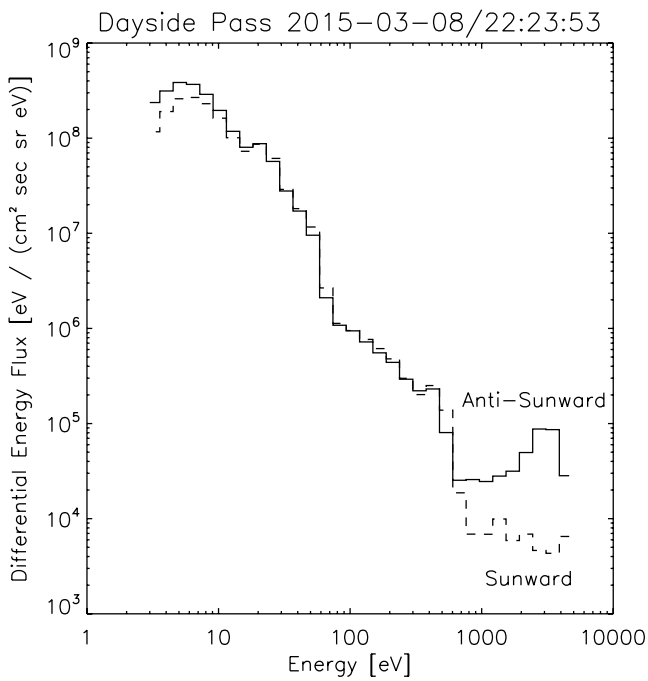

Figure 3. Time–averaged flux–energy spectra for sunward (dashed) and anti–sunward (solid) particle velocities. The fluxes were averaged over times where the spacecraft altitude was below 300 km, during a Mars Atmosphere and Volatile EvolutioN periapsis pass on 08 March 2015. At energies above ∼800 eV the two spectra diverge, revealing a population of negatively charged particles with anti–sunward velocities, with a peak near ∼3 keV.

It is worth noting that the data shown in Figure 1 was taken during a MAVEN orbit that followed a high–speed interplanetary coronal mass ejection (CME). The CME dramatically increased the number of charged particles incident on the Martian exosphere, leading to a significant increase in the penetrating ENA flux and subsequently a significant increase in the H^- flux observed at low altitudes. During times with more typical solar wind conditions, both the energy and flux of the low–altitude H^- population were lower than seen in Figure 1 (and sometimes were not detectable at all). We chose to use the above orbit as an example because of the clarity of the H^- signal and the clear difference in flux between the sunward and anti–sunward velocity directions.

3. Flux–Energy Spectra

For every orbit in our analysis, we averaged the flux measured by SWEA during times when the spacecraft altitude was below 300 km, for both the sunward and anti–sunward velocity directions. The altitude upper limit of 300 km was chosen so that our analysis would not include solar wind electrons present at altitudes upstream of the bow shock. Plotting the averaged fluxes against the detector energies, we created time–averaged flux–energy spectra. Figure 3 shows both the sunward (dashed) and anti–sunward (solid)

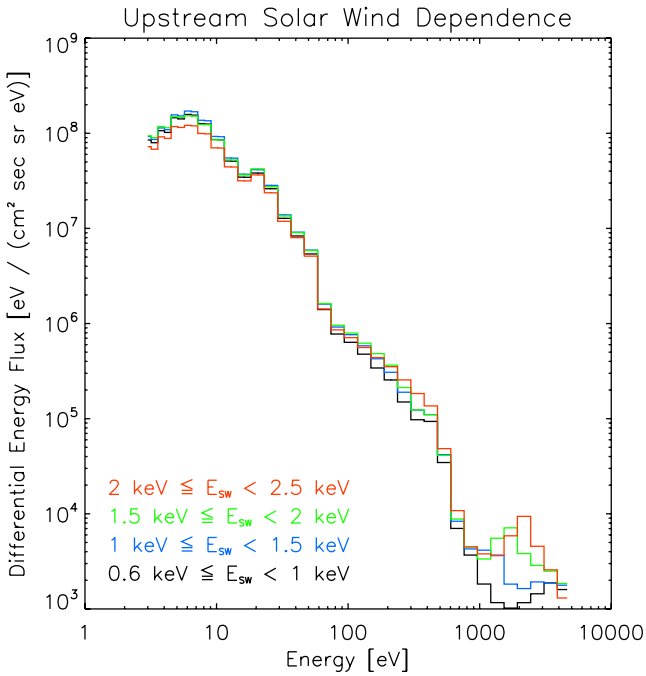

Figure 4. Four flux–energy spectra, averaged over solar wind energies. The spectra were calculated using the background–corrected anti–sunward spectra of the individual orbits. H^- ions were detected above ~800 eV for solar wind energies above 1 keV. At higher solar wind energies, both the peak flux and the peak energy of the H^- ions increase.

flux–energy spectra for a MAVEN orbit on 08 March 2015 (the same orbit used in Figure 1). Visible in both spectra are peaks around ~20 eV from photoionization of CO_2 and O (Frahm et al., 2006), and ~500 eV from Auger electrons produced by *K* shell ionization of atmospheric gases (Mitchell et al., 2000; Sakai et al., 2015). Above ~800 eV the two spectra diverge, with a peak in the anti–sunward spectrum around ~3 keV corresponding to H^- ions produced by solar wind ENA reconversion.

We do not expect to see any significant flux of negatively charged particles at high energies and low altitudes in the sunward velocity direction. Although some H^- ions may experience enough collisions to be backscattered into the sunward velocity direction, the expected energy loss from such collisions would cause the backscatter fluxes to be obscured by the high fluxes of electrons. Combined with the low flux of H^- ions to begin with, it is unlikely that we would be able to detect any backscattered H^-. We therefore considered the high–energy flux seen in the sunward velocity direction to be entirely background, resulting from natural radioactivity in the microchannel plate detectors and/or penetrating galactic cosmic rays. For each orbit in our analysis, we calculated the background flux by averaging the flux measured in the four highest detector energy bins for the sunward velocity direction. Some orbits in our analysis were missing data at high energy sunward data. In order to ensure that all orbits had some background subtraction applied, we used as the background for these orbits the average value calculated from all other orbits. Although the background flux is not necessarily consistent between orbits, this issue only applies to a small fraction of the orbits used in our analysis. We corrected the measured anti-sunward fluxes by subtracting the calculated background. These background-subtracted fluxes were used to examine all spectra described in this paper.

The monodirectional velocities of the H^- ions that SWEA observed at energies above ~800 eV are indicative of particles with origins in the solar wind. Therefore, we expect the fluxes and energies of these H^- ions to depend on the conditions of the upstream solar wind. SWIA measured the solar wind with both direct observations of upstream solar wind protons and observations of penetrating protons in the atmosphere converted to an estimate of the upstream solar wind. We grouped MAVEN orbits based on the upstream solar wind energy measured by SWIA during each orbit and averaged the SWEA background–corrected anti–sunward flux–energy spectra for each solar wind energy group. Figure 4 shows four flux–energy spectra corresponding to four solar wind energy ranges, which together contain all 3150 MAVEN orbits used in our study. Below detector energies of ~800 eV the spectra are dominated by fluxes of photoelectrons, which are independent of the solar wind. The familiar H^- signal shows up at solar wind energies greater than 1 keV, suggesting that solar wind protons must have sufficiently high energy to produce H^- ions that are detectable above the electron fluxes. As the upstream solar wind energy increases, both the peak flux and the peak energy of the H^- ions increase.

4. Seasonal Variation

Over the course of the Martian year, the neutral hydrogen column density upstream of the bow shock varies significantly, with the highest densities occurring near perihelion and the southern summer solstice (Clarke et al., 2014; Halekas, 2017). The flux of hydrogen ENAs produced by charge exchange is proportional to the neutral density, as discussed by Burch et al. (2015). Because the flux of H^- ions should depend on the flux of ENAs, we expect to observe increased fluxes of H^- ions during times of increased neutral density. We binned MAVEN orbits by Martian solar longitude and calculated the average differential energy flux of H^- for each bin, identifying the H^- differential energy flux for each orbit as the peak differential energy flux measured by SWEA above 1 keV. Figure 5 shows the average differential energy flux of H^- at each solar longitude bin, with each bin spanning 60° in L_S. At high L_S, the H^- differential energy flux is increased by a factor of ~2, with the highest average differential energy flux seen between $L_S = 240°$ and $L_S = 300°$. This range contains perihelion and the southern summer

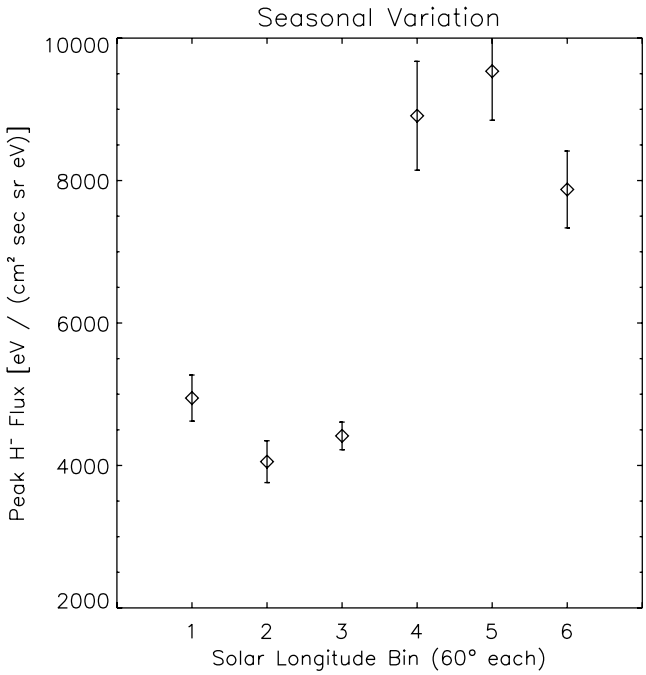

Figure 5. Average differential energy flux of H^- ions for 6 Martian solar longitude bins. Each bin spans 60° of L_S, or two Martian months. Average differential energy fluxes were calculated using the peak differential energy flux measured by Solar Wind Electron Analyzer above 1 keV. The flux of H^- ions increased by a factor of ~2 at high L_S, with a maximum occurring at $240° \leq L_S \leq 300°$. Error bars correspond to the standard error of the mean.

solstice, where the highest fluxes are expected. The seasonal increase in H^- flux coincides with the seasonal increase in neutral density, and the factor ~2 increase is reasonable given the change in exospheric neutral column density calculated by Halekas (2017). When calculating the average H^- differential energy flux in Figure 5, we considered all particle energies above 1 keV. Although the H^- flux is dependent on energy (as discussed previously), there is no systematic dependence of the solar wind energy (and therefore the H^- energy) on the Martian season. In general, variations in the solar wind energy take place on shorter time scales (days or weeks) or on longer time scales (solar cycle). Although the data used in this analysis covers roughly half of the solar cycle and the solar wind energy may vary over that time, those variations occur much more slowly than the observed variations in differential energy flux over the Martian year. Therefore, the variation in differential energy flux seen in Figure 5 does not reflect a variation in the upstream solar wind energy.

5. Charge State Density Ratios

Hydrogen ENAs streaming through the collisional atmosphere experience electron stripping and electron attachment in collisions with atmospheric gas, producing H^+ ions and H^- ions, respectively. The relative abundance of each charge state was measured at comet 67P (Burch et al., 2015), where the fluxes of H^- were ~10% of the fluxes of H^+. Early observations at Mars by MAVEN (Halekas, Lillis, et al., 2015) also found H^- fluxes that were ~10% that of H^+ fluxes. We examined the relative amounts of each charge state by comparing the densities of H^- measured by SWEA to the densities of H^+ measured by SWIA.

The density moment n is calculated from the velocity distribution function $f(v)$ by

$$n = \int f(v)\,\mathrm{d}^3v = \int f(v)\,v^2\,\mathrm{d}v\,\mathrm{d}\Omega = \int f(v)\sqrt{\frac{2E}{m^3}}\,\mathrm{d}E\,\mathrm{d}\Omega, \tag{1}$$

where v is velocity, E is energy, m is mass, and Ω is solid angle. The conversion from velocity distribution function $f(v)$ to differential energy flux F is

$$f(v) = \frac{m^2}{2E^2}F. \tag{2}$$

Therefore, the density moment n can be calculated from differential energy flux F by

$$n = \int \sqrt{\frac{m}{2}}\,E^{-3/2}\,F\,\mathrm{d}E\,\mathrm{d}\Omega\,. \tag{3}$$

Since SWEA measured the differential energy flux F of particles with discrete energy ranges, we computed the density moment n of H^- ions using a weighted sum,

$$n = \sqrt{\frac{m}{2}}\,\Delta\Omega \sum E^{-3/2}\,\Delta E\,F, \tag{4}$$

where m is the mass of hydrogen, $\Delta\Omega = \pi/\sqrt{2}$ is the solid angle covered by the measurement, E is the observed particle energy, ΔE is the width of the energy bin, and the sum is over energy bins above 800 eV. We computed the average density using all 3,150 orbits. Although there may be little to no flux of H^- for orbits where the solar wind energy was below 1 keV (see Figure 4), the energy cutoff of 800 eV ensures that the H^- ions are distinguishable from atmospheric electrons. Therefore, the computed density accurately reflects the amount of H^- ions observed. The average H^- density was 1.416×10^{-4} particles/cm^3. The density of H^+ ions (which are produced

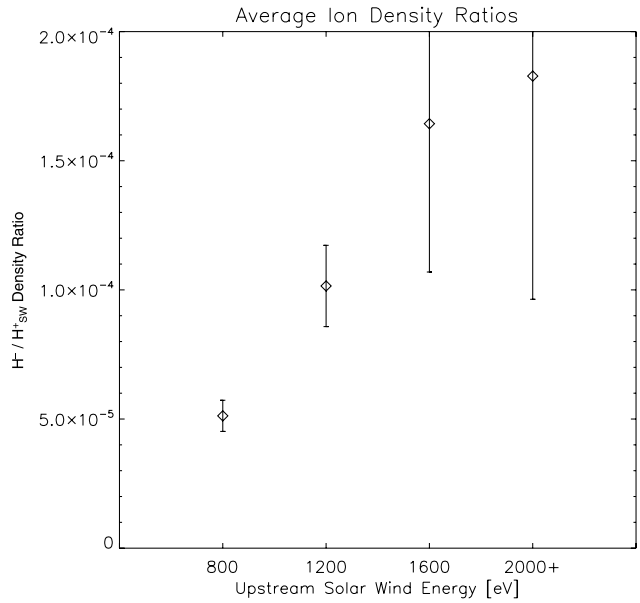

Figure 6. Average ratios of H^- density to solar wind proton density for four solar wind energy bins, each covering 400 eV. H^- densities were calculated with Solar Wind Electron Analyzer differential energy fluxes measured above 800 eV. Solar wind proton densities and energies were measured by Solar Wind Ion Analyzer. Error bars correspond to the standard error of the mean.

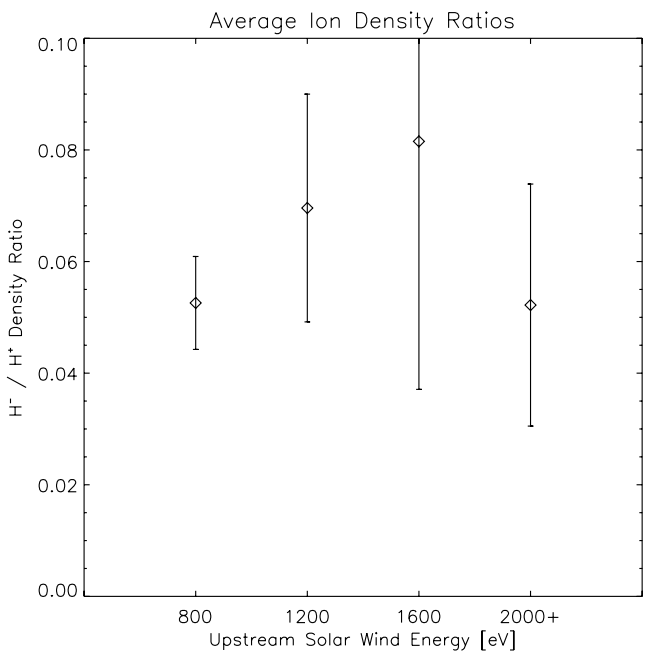

Figure 7. Average H^-/H^+ density ratios for four solar wind energy bins, each 400 eV wide. H^- densities were calculated using Solar Wind Electron Analyzer differential energy fluxes, and H^+ densities were calculated using Solar Wind Ion Analyzer penetrating proton measurements. Error bars correspond to the standard error of the mean.

in the collisional atmosphere in the same manner as the H^- ions) was calculated similarly using the flux measurements made by SWIA (Halekas, Lillis, et al., 2015). The ratio of the average H^- density to the average H^+ density was ~4%. This ratio is that of the densities averaged over all 3,150 orbits.

While collisions between ENAs and atmospheric gases produce H^- ions and H^+ ions, backreactions also occur, converting H^- and H^+ back to a neutral state. The amounts of H^- and H^+ present at a given time are ultimately determined by the relevant cross sections (electron capture for H^-, electron loss for H^+) and backreactions (photodetachment and charge exchange for H^-, primarily charge exchange for H^+). Laboratory measurements indicate a ratio of ~10% between the electron capture and electron loss cross sections in collisions between 1 keV H and CO_2 (Lindsay et al., 2005). If the backreactions for H^- and H^+ occurred at similar rates, we would expect the ratio between H^- density and H^+ density to also be ~10%. The lower ratio of ~4% that we observed suggests that backreactions more quickly convert H^- to H than charge exchange converts H^+ to H.

Ion production in CO_2 dominated atmospheres is mostly carried out by collisions between neutral hydrogen and carbon dioxide (Kallio & Barabash, 2001). Laboratory experiments performed by Lindsay et al. (2005) measured the cross sections for electron loss and electron capture in collisions between H and CO_2 and found that both cross sections increase with the energy of the incident H atom. The analogous situation at Mars involves solar wind hydrogen ENAs incident upon atmospheric CO_2. We used the ratio between H^- density and solar wind proton (H^+_{SW}) density as a measure of the electron capture cross section, and the upstream solar wind energy as a measure of the incident H energy. The density and energy of the upstream solar wind were measured by SWIA. Figure 6 shows the H^-/H^+_{SW} density ratio as a function of the upstream solar wind energy. We observed a factor of ~4 increase in the H^-/H^+_{SW} density ratio, a trend that compares favorably with Lindsay et al. (2005). Between an upstream solar wind energy of 1,200 eV and 2,000+ eV, where the H^- ions are more easily distinguished from thermal electrons, this factor was ~2. We also examined how the ratio between H^- density and penetrating proton (H^+) density varies with solar wind energy, as shown in Figure 7. We found a flatter trend overall, which is expected since both the electron loss and electron capture cross sections increase with incident H energy. Each point in Figures 6 and 7 corresponds to the density ratio, averaged over the number of orbits in their respective energy bin.

6. Conclusions

MAVEN observed a population of negatively charged particles at periapsis altitudes in Mars' collisional atmosphere. The energy, angular distribution, and dependence on the upstream solar wind of these particles were consistent with H^- ions produced in collisions between solar wind H ENAs and atmospheric CO_2. The flux of H^- varied seasonally along with the neutral hydrogen column density upstream of the bow shock, indicating that the penetrating hydrogen ENAs likely formed through charge–changing interactions between solar wind protons and exospheric hydrogen atoms.

We calculated relative abundances of H^- ions that were similar to, although slightly smaller than, previous work at both Mars and at comet 67P/Churyumov–Gerasimenko. The smaller ratio between H^- density and

penetrating proton density suggests that conversion of H^- back to H (through photodetachment, charge exchange) may occur more quickly than conversion of H^+ to H (primarily through charge exchange). In future work, a Monte–Carlo model could be used to track different charged species through the collisional atmosphere, taking into account the relevant reactions (collisions, charge exchange, photodetachment). Such a model could provide a useful comparison to the measured relative charge state abundances presented here. Future work could also estimate the equilibrium charged fraction, and the related detachment cross section, of H^- ions in the atmosphere using the observed H^-/H^+_{SW} density ratio. Such models could provide insight into the various interactions that occur between charged species in the collisional atmosphere.

Data Availability Statement

The datasets used in the analysis described in this manuscript are available for download on zenodo.org (Jones, 2021).

Acknowledgments
We acknowledge the Mars Atmosphere and Volatile EvolutioN contract and the Solar System Workings program through grant NNX16AO84G for support.

References

Anderson, D. E. (1974). Mariner 6, 7, and 9 ultraviolet spectrometer experiment: Analysis of hydrogen Lyman alpha data. *Journal of Geophysical Research*, *79*(10), 1513–1518. https://doi.org/10.1029/JA079i010p01513

Bisikalo, D. V., Shematovich, V. I., Gérard, J.-C., & Hubert, B. (2018). Monte Carlo simulations of the interaction of fast proton and hydrogen atoms with the Martian atmosphere and comparison with in situ measurements. *Journal of Geophysical Research: Space Physics*, *123*(7), 5850–5861. https://doi.org/10.1029/2018JA025400

Brinkfeldt, K., Gunell, H., Brandt, P. C., Barabash, S., Frahm, R. A., Winningham, J. D., et al. (2006). First ENA observations at Mars: Solar-wind ENAs on the nightside. *Icarus*, *182*(2), 439–447. https://doi.org/10.1016/j.icarus.2005.12.023

Burch, J. L., Cravens, T. E., Llera, K., Goldstein, R., Mokashi, P., Tzou, C.-Y., & Broiles, T. (2015). Charge exchange in cometary coma: Discovery of H^- ions in the solar wind close to comet 67P/Churyumov-Gerasimenko. *Geophysical Research Letters*, *42*(13), 5125–5131. https://doi.org/10.1002/2015GL064504

Chaufray, J. Y., Bertaux, J. L., Leblanc, F., & Quémerais, E. (2008). Observation of the hydrogen corona with SPICAM on Mars Express. *Icarus*, *195*(2), 598–613. https://doi.org/10.1016/j.icarus.2008.01.009

Clarke, J. T., Bertaux, J.-L., Chaufray, J.-Y., Gladstone, G. R., Quemerais, E., Wilson, J. K., & Bhattacharyya, D. (2014). A rapid decrease of the hydrogen corona of Mars: The Martian Hydrogen Corona. *Geophysical Research Letters*, *41*(22), 8013–8020. https://doi.org/10.1002/2014GL061803

Deighan, J., Jain, S. K., Chaffin, M. S., Fang, X., Halekas, J. S., Clarke, J. T., et al. (2018). Discovery of a proton aurora at Mars. *Nature Astronomy*, *2*(10), 802–807. https://doi.org/10.1038/s41550-018-0538-5

Frahm, R. A., Winningham, J. D., Sharber, J. R., Scherrer, J. R., Jeffers, S. J., Coates, A. J., et al. (2006). Carbon dioxide photoelectron energy peaks at Mars. *Icarus*, *182*(2), 371–382. https://doi.org/10.1016/j.icarus.2006.01.014

Futaana, Y., Barabash, S., Grigoriev, A., Holmström, M., Kallio, E., Brandt, P. C., et al. (2006). First ENA observations at Mars: ENA emissions from the Martian upper atmosphere. *Icarus*, *182*(2), 424–430. https://doi.org/10.1016/j.icarus.2005.09.019

Girazian, Z., & Halekas, J. (2021). Precipitating solar wind hydrogen at Mars: Improved calculations of the backscatter and Albedo with MAVEN observations. *Journal of Geophysical Research: Planets*, *126*(2), e2020JE006666. https://doi.org/10.1029/2020JE006666

Gunell, H., Brinkfeldt, K., Holmström, M., Brandt, P. C., Barabash, S., Kallio, E., et al. (2006). First ENA observations at Mars: Charge exchange ENAs produced in the magnetosheath. *Icarus*, *182*(2), 431–438. https://doi.org/10.1016/j.icarus.2005.10.027

Halekas, J. S. (2017). Seasonal variability of the hydrogen exosphere of Mars: Mars hydrogen. *Journal of Geophysical Research: Planets*, *122*(5), 901–911. https://doi.org/10.1002/2017JE005306

Halekas, J. S., Lillis, R. J., Mitchell, D. L., Cravens, T. E., Mazelle, C., Connerney, J. E. P., et al. (2015). MAVEN observations of solar wind hydrogen deposition in the atmosphere of Mars. *Geophysical Research Letters*, *42*(21), 8901–8909. https://doi.org/10.1002/2015GL064693

Halekas, J. S., Taylor, E. R., Dalton, G., Johnson, G., Curtis, D. W., McFadden, J. P., et al. (2015). The solar wind ion analyzer for MAVEN. *Space Science Reviews*, *195*(1–4), 125–151. https://doi.org/10.1007/s11214-013-0029-z

Holmström, M. (2002). Energetic neutral atoms at Mars 1. Imaging of solar wind protons. *Journal of Geophysical Research*, *107*(A10), 1277. https://doi.org/10.1029/2001JA000325

Jones, N. (2021). MAVEN observations of H− ions at Mars (Dataset) [Data set]. Zenodo. https://doi.org/10.5281/zenodo.5090786

Kallio, E., & Barabash, S. (2001). Atmospheric effects of precipitating energetic hydrogen atoms on the Martian atmosphere. *Journal of Geophysical Research*, *106*(A1), 165–177. https://doi.org/10.1029/2000JA002003

Kallio, E., Luhmann, J. G., & Barabash, S. (1997). Charge exchange near Mars: The solar wind absorption and energetic neutral atom production. *Journal of Geophysical Research*, *102*(A10), 22183–22197. https://doi.org/10.1029/97JA01662

Lindsay, B. G., Yu, W. S., & Stebbings, R. F. (2005). Cross sections for charge-changing processes involving kilo-electron-volt H and H + with CO and CO_2. *Physical Review A*, *71*(3), 032705. https://doi.org/10.1103/PhysRevA.71.032705

Mitchell, D. L., Lin, R. P., Rème, H., Crider, D. H., Cloutier, P. A., Connerney, J. E. P., et al. (2000). Oxygen Auger electrons observed in Mars' ionosphere. *Geophysical Research Letters*, *27*(13), 1871–1874. https://doi.org/10.1029/1999GL010754

Mitchell, D. L., Mazelle, C., Sauvaud, J.-A., Thocaven, J.-J., Rouzaud, J., Fedorov, A., et al. (2016). The MAVEN solar wind electron analyzer. *Space Science Reviews*, *200*(1–4), 495–528. https://doi.org/10.1007/s11214-015-0232-1

Mura, A., Orsini, S., Milillo, A., Kallio, E., Galli, A., Barabash, S., et al. (2008). ENA detection in the dayside of Mars: ASPERA-3 NPD statistical study. *Planetary and Space Science*, *56*(6), 840–845. https://doi.org/10.1016/j.pss.2007.12.013

Ritter, B., Gérard, J.-C., Hubert, B., Rodriguez, L., & Montmessin, F. (2018). Observations of the proton aurora on Mars with SPICAM on board Mars express. *Geophysical Research Letters*, *45*(2), 612–619. https://doi.org/10.1002/2017GL076235

Sakai, S., Rahmati, A., Mitchell, D. L., Cravens, T. E., Bougher, S. W., Mazelle, C., et al. (2015). Model insights into energetic photoelectrons measured at Mars by MAVEN. *Geophysical Research Letters*, *42*(21), 8894–8900. https://doi.org/10.1002/2015GL065169

Shematovich, V. I., Bisikalo, D. V., Diéval, C., Barabash, S., Stenberg, G., Nilsson, H., et al. (2011). Proton and hydrogen atom transport in the Martian upper atmosphere with an induced magnetic field. *Journal of Geophysical Research*, *116*(A11), A11320. https://doi.org/10.1029/2011JA017007

Wang, X.-D., Barabash, S., Futaana, Y., Grigoriev, A., & Wurz, P. (2013). Directionality and variability of energetic neutral hydrogen fluxes observed by Mars Express. *Journal of Geophysical Research: Space Physics*, *118*(12), 7635–7642. https://doi.org/10.1002/2013JA018876